# Highly directional emission from a quantum emitter embedded in a hemispherical cavity

# Highly directional emission from a quantum emitter embedded in a hemispherical cavity

**Y. Ma[1], G. Ballesteros[1], J. M. Zajac[1], J. Sun[2], and B. D Gerardot[1]***

[1]*Institute of Photonics and Quantum Sciences, SUPA, Heriot-Watt University, Edinburgh, EH14 4AS, UK*

[2]*Institute of Mechanical, Process and Energy Engineering, Heriot-Watt University, Edinburgh, EH14 4AS, UK*

*Email: y.ma@hw.ac.uk, b.d.gerardot@hw.ac.uk*

We report the design of a solid-state, micron-sized hemispherical cavity which yields significantly enhanced extraction efficiency with modest Purcell enhancement from embedded quantum emitters. A simple analytical model provides a guideline for the design and optimization of the structure while finite-difference time-domain simulations are used for full analysis of the optimum structure. Cavity modes with up to 90% extraction efficiency, a Purcell enhancement factor > 2, and a quality factor of ≈50 are achieved. In addition, Gaussian-like far-field beam profiles with low divergence are exhibited for several modes. These monolithic cavities are promising for solid-state emitters buried in a high dielectric environment, such as self-assembled quantum dots and optically active defects in diamond.

Optimizing the transfer of light to and from a quantum emitter is paramount in the emerging field of quantum photonics. One approach to improve the light-matter interaction for an emitter buried in a solid-state environment is the use of a hemispherical solid-immersion lens (SIL) [1]. A SIL effectively functions as an optical antenna which increases the conversion efficiency between far-field optical radiation and the quantum system, and vice versa. The photon extraction efficiency ($\eta_{ex}$) into an objective lens is improved due to an increased effective numerical aperture ($NA_{eff}$) and increased critical angle for escaping light [2-7]. Concurrently, the larger $NA_{eff}$ improves the diffraction limited resolution, increasing the extinction efficiency of far-field resonant radiation [8-10]. To maximize a hemisphere SIL's performance, it should be fabricated out of a material with the highest possible refractive index ($n$) that is transparent at the required optical frequency, e.g. GaAs [9] or GaP [11] for $\lambda$ < 1 μm. However, even in the best case scenario $\eta_{ex}$ is limited to 50% for a dipole buried in a bulk sample as half of the light is radiated downward (away from the SIL and collection optics). An obvious solution to this is to reflect this light back towards the SIL with a mirror. In this case, a low-Q planar cavity between the mirror and semiconductor – SIL interface is formed which modifies the radiation pattern [12-15]. Unfortunately, even for optimized second order cavity structures, radiation escapes via in-plane guided modes and $\eta_{ex}$ is far less than unity. To reduce the light lost via these guided modes, in-plane mode confinement is required. Many successful approaches to implement lateral confinement have been demonstrated, often resulting in high-Q's and small mode volumes [16]. However, such approaches do not necessarily result in highly directive far-field radiation patterns. Further, broadband performance is desirable for many applications.

In this Letter, we theoretically investigate the reduction of the hemisphere SIL from macroscopic to microscopic size to reduce the planar cavity leaky modes and increase the directivity of the dipole's radiation pattern. We find that optimized structures can have modest quality ($Q$) modes that simultaneously yield Gaussian-like far-field radiation patterns with high $\eta_{ex}$, modest Purcell factors ($F_P$), and relatively broadband operation. This promising design is readily applicable to commonly used quantum emitters, in particular defect centers in diamond and self-assembled III-V quantum dots, which we consider in detail here. Our design consists of a single horizontal dipole source with emission at 950 nm (typical properties of InGaAs quantum dots) embedded between a GaAs membrane (with thickness $h$ = 185 nm) and a hemisphere GaAs μ-SIL (with radius $r$ of the order of the emission wavelength $\lambda$) as shown in Figure 1(a). The quantum emitter is located at the center of the hemispherical μ-SIL which can be precisely positioned using 2D photoluminescence imaging technique [17]. Below the GaAs membrane is a Au back reflection layer with high reflectance at 950 nm (> 98%) [18]. The membrane thickness is chosen to keep the dipole at an antinode position along the longitudinal axis ($z$-axis) of the cavity for the designed wavelength range, 920 nm < $\lambda$ < 980 nm. The thickness of the Au layer, $d$, is kept large enough to prevent any leakage through it (e.g. $d$ = 200 nm). The planar Au layer and hemispherical GaAs-vacuum interface form a weak cavity with a low $Q$ and small mode volume. A bulk GaAs substrate is placed underneath to provide rigidity to the membrane.

To gain insight into how our design operates and achieves highly directive radiation patterns, we first develop a simple analytical model which also provides a fast way to prototype and explore the design parameter space efficiently. The model is closely related to the one used in ref. [19] to model the properties of macroscopic

SILs. We consider the schematic in Fig. 1(a), in which four rays emerge from the center of the hemisphere where the dipole is located. Rays traced from the center of the hemisphere are normal to the surface and do not suffer refraction upon transmission. It is clear from the diagram that in general rays will not form a closed loop going back and forth inside the hemisphere, in contrast with the results of [19]. Angle $\gamma$ in Fig.1(a) can be used to quantify how much their trajectories diverge from a closed path:

$$\sin\gamma = \frac{2h}{r}\sin(\Phi) \tag{1}$$

$$\alpha(\Phi) = \frac{2h}{\cos\Phi} \tag{2}$$

where angle $\Phi$ is indicated in Fig.1(a) and $\alpha$ is the distance traveled by a ray when it crosses the slab. The design point of the final structure is selected in such a way that $r >> h$. In this circumstance, the rays trace an almost closed path during the first few reflections. Considering that the reflectivity at the GaAs-vacuum interface is ≈ 30%, only the first few reflections will contribute significantly to the outwards radiation. Our model remains valid under these two assumptions ($r >> h$ and high losses). Combining the formalisms presented in [20] and [21], we derive an equation for the radiation pattern emitted from the device when excited by a dipole placed at the center of the hemisphere. We assume that all rays emerging from the center of the hemisphere follow closed paths and are reflected back to it, going back and forth as they propagate. As $0 < \theta < \pi/2$, we add up the contributions of the dipole radiation being emitted both at positive and negative angles. Four main rays (and their reflections) will contribute to the final field in a given direction, as shown in Fig.1(a). Finally, we introduce an angle dependent phase for the reflection from the bottom Au mirror that accounts for the offset between the hemisphere center and the Au back mirror. Considering an infinite number of contributions (but remembering that only the first few terms dominate) we arrive at a power sum $E_{rad}$ that can be solved analytically resulting in:

$$E_{rad} = \begin{bmatrix} 1 + l' \exp(jk(\alpha + r)) \\ + l'^2 l \exp(jk(2\alpha + r)) \\ + l l' \exp(jk(2\alpha + r)) \end{bmatrix} \frac{E_0 t}{1 - (l' l \exp(jk(\alpha + r)))^2} \tag{3}$$

where $k$ is the wavevector in GaAs, $E_0$ is the field intensity of the dipole source, $t$ and $l$ ($l'$) the transmission and reflection Fresnel coefficients [21] on the GaAs-air (GaAs-Au) interface. The first multiplying term in parenthesis contains the contribution of the main rays to the final field. The SIL radius ($r$) is rescaled to a reduced cavity radius $R$ in the GaAs medium at the central wavelength ($\lambda$ = 950 nm): $R = (r \cdot n_{GaAs})/950$. The refractive indices of GaAs and Au (at T = 4 K and $\lambda$ = 950 nm) from references [18] and [22] are used, respectively.

Figure 1(b) shows a map of the power sum $E_{rad}$ in the '$\theta$ = 0' direction as function of $R$ and $\lambda$ obtained using the analytical model. There are several discrete resonance modes labeled as $M^n$ (where $n$ = 1, 2 ...8). Each mode corresponds to the constructive interference of light emerging normally from the sample. The peak of each resonant mode moves to longer $\lambda$ as $R$ increases. For a specific λ, the resonance modes are separated by $R$ = 0.5, indicating that the μ-SIL can be approximated as an ensemble of conventional Fabry-Perot (FP) cavities with an angle ($\theta$) dependent effective cavity length. The radiation pattern can also be obtained (not shown) using this analytical method and the approach of Trentini [20].

While the analytical model provides a good approximation and an intuitive understanding of the cavity's performance, its accuracy is limited by the assumptions. Therefore, we use finite difference time domain (FDTD) simulations to calculate $\eta_{ex}$, $F_p$, the power flux $\eta_{pf}$ ($\eta_{pf} = \eta_{ex} \cdot F_p$) and far field power density $P_\theta$ for a range of $R$ and $\lambda$. It is known that for typical spherical cavities, the emission modes are predominantly characterized by two orthogonal polarized modes (*TE* and *TM*) [23]. Since the cavity has axial symmetry, the overall emission efficiency can be characterized by integrating $P_\theta$ over the spherical space for TE and TM modes respectively. To separately analyze the emission properties of both TE and TM modes, we perform a two-dimensional (2D) simulation in the $S_{TE}$ and $S_{TM}$ planes, as shown in Figure 1 (d) [24]. $S_{TM}$ ($S_{TE}$) is parallel (orthogonal) to the dipole orientation, enabling only *TM* (*TE*) mode excitation. As shown in Fig. 2(a), there are several discrete modes in the μ-SIL as a function of $\lambda$ and $R$ (labeled as $TE_n^m$ and $TM_n^m$ where $m$ and $n$ indicate the main modes and sub-modes, respectively). For a specific emission wavelength (e.g. $\lambda$ = 950 nm), the peak positions of the main modes have an oscillation period of ≈ 0.5$R$ (see Figure 2(b)) and quantitatively match the analytical results. These modes correspond to an equivalent cavity order, comparable to the longitudinal modes in a planar cavity [24]. The sub-modes show characteristics similar to transverse modes in a FP resonator. While the peak positions of *TE* and *TM* modes are typically shifted slightly with respect to each other due to the sub-modes, at certain $R$ and $\lambda$ the peak positions collide (see Fig. 2(b) and (c)); these positions are considered the optimal design point for the cavity. Fig. 2(c) also demonstrates the broad-bandwidth of the cavity modes: the bandwidth $\Delta\lambda$ of *TE* and *TM* resonance modes at $\lambda$ = 950 nm is ≈ 20 nm (FWHM). A final important characteristic of the μ-SIL is the far-field distribution of the radiation. Fig. 2(d) shows the simulated far-field distribution for various *TE* and *TM* modes at $\lambda$ = 950 nm. Varying far-field beam profiles are observed for each mode and the divergence of the highly directive far-field beam pattern decreases as the effective cavity order increases. For example, the far-field divergence of modes $TE_n^5$ and $TM_n^5$ is ≈ 5°, corresponding to NA ≈ 0.1. Such a Gaussian-like beam pattern with low divergence is important for efficiently coupling radiation to a single mode fiber.

To validate these results and more accurately characterize the μ-SIL performance, we perform full

three-dimensional (3D) FDTD simulations. The 3D simulation region has a size of 10 x 10 x 2 $\mu m^3$ and a structured mesh with a cell size of 10 nm is used. Perfectly matched layer boundary conditions are applied to the simulation domain. We first analyze $\eta_{pf}$ as a function of $R$ and $\lambda$, as shown in Fig. 3(a). The 3D results generally agree with the 2D and analytical results. It is assumed that the discrete modes include both TE and TM polarization components and the maximum of the resonance occurs at the value of $R$ where a *TE* and *TM* mode superimpose. We label the resonance modes as $M^i_j$, where $i$ ($j$) corresponds to the main (sub-) mode. At the design wavelength ($\lambda$ = 950 nm), $\eta_{pf}$, $F_p$ and $\eta_{ex}$ oscillate with $R$, the resonances belong to several main modes ($M_n^3$, $M_n^4$, ... $M_n^{11}$) with a period of ≈ 0.5$R$, as shown in Figure 3(b). The maxima for both $\eta_{pf}$ and $F_p$ are found at $R$ = 4.3 while the maximum $\eta_{ex}$ exists at $R$ = 3.3. The envelope of the $\eta_{pf}$ oscillations shows a dip at $R$ = 3.3 due to reduced $F_p$ caused by increased coupling to leaky modes occurring at the spherical surface of the μ-SIL and guided modes in the membrane, as designated by the green arrows in Fig. 1(c). Fig. 3(c) shows $\eta_{pf}$ as a function of $\lambda$ for various values of $R$. The peak positions center around $\lambda$ = 950 nm with a variation of ≈ 10 nm, but could be more precisely located at $\lambda$ = 950 nm using smaller step sizes in $R$ for the simulation. The spectral bandwidth for the modes is ≈ 20 nm, in good agreement with 2D simulation and analytical model results. Fig. 3(d) shows the far-field distribution for several modes. For lower order modes, the far-field shows multiple side-bands while higher order modes show Gaussian-like far-field patterns with low divergence. The divergence decreases with increasing effective cavity order. On the other hand, increasing $R$ increases the effective mode volume and therefore decreases $F_p$. This trade-off between the optimized Purcell enhancement and far-field beam pattern could perhaps be further minimized by varying the geometric parameters of the μ-SIL, such as the position of the QD and the membrane thickness ($h$ in Fig. 1(a)).

Fig. 4 shows $\eta_{pf}$ and $\eta_{ex}$ for various resonance modes as a function of NA. As expected by examining the far-field beam profiles of the higher-order modes (e.g. $M_2^5$, $M_2^6$, $M_2^7$, and $M_2^8$), both parameters plateau between 0.4 < NA < 0.7. This regime is promising for practical cryogenic-compatible confocal microscopes. For greater NA, the high divergence components can be collected and $\eta_{ex} \rightarrow 0.9$ with $\eta_{pf} \rightarrow 2.3$ for mode $M_2^6$. Conversely, the large divergence observed in Fig. 3(d) for mode $M_2^4$ leads to significantly worse performance compared to the higher cavity order modes. Further details of the figures of merit for selected modes can be found in Table 1. Finally, we also analyzed a μ-SIL on a bulk substrate (e.g. without the membrane and Au reflection layer) as shown in Fig. 3(d) and Fig. 4. Both $\eta_{pf}$ and $\eta_{ex}$ for mode $M^6_{no\_Au}$ (0.29 and 0.18, respectively, for NA = 1.0) are much worse than those of the resonances in the μ-SIL with the membrane and Au reflection layer. In fact, these figures of merit are much worse than expected for a GaAs *macro*-SIL on a bulk substrate [3]. This demonstrates that the thin membrane and highly reflective layer Au layer are essential to obtain good performance with a μ-SIL.

In summary, we have designed a monolithic micro-cavity that produces highly directive emission and modest Purcell enhancement for emission from a solid-state two level system. Due to the Rayleigh-Carson reciprocity theorem, such a device will also enable strong extinction of incident far-field resonant radiation by the quantum emitter. As an example of monolithic hemisphere fabrication, we show in Fig. 1(d) a scanning electron micrograph of a GaAs μ-SIL fabricated using a water-assisted focused ion beam (FIB). An alternative fabrication approach is selective oxidation of a composition-graded digital alloy of AlGaAs [25]. Micro-SILs have also been fabricated in diamond via FIB [5]. An advantage of a monolithic μ-SIL cavity is the elimination of potential air-gaps at the membrane-SIL interface. Further, such structures are compatible with electric contacts to electrically pump and manipulate the quantum emitter.

We acknowledge financial support from a Royal Society University Research Fellowship, the EPSRC (EP/I023186/1, EP/K015338/1, and EP/M013472/1), and an ERC Starting Grant (No. 307392).

1. S. M. Mansfield, G. S. Kino, Appl. Phys. Lett. **57**, 2615 (1990).
2. K. Koyama, M. Yoshita, M. Baba, T. Suemoto and H. Akiyama, Appl. Phys. Lett. **75**, 1667 (1999).
3. V. Zwiller and G. Bjork, J. Appl. Phys. **92**, 660 (2002).
4. S. Moehl, H. Zhao, B. Dal Don, S. Wachter and H. Kalt, J. Appl. Phys. **93**, 6265 (2003).
5. J. P. Hadden, J. P. Harrison, A. C. Stanley-Clarke, L. Marseglia, Y.-L. D. Ho, B. R. Patton, J. L. O'Brien and J. G. Rarity, Appl. Phys. Lett. **97**, 241901 (2010).
6. P. Siyushev, F. Kaiser, V. Jacques, I. Gerhardt, S. Bischof, H. Fedder, J. Dodson, M. Markham, D. Twitchen, F. Jelezko, and J. Wrachtrup, Appl. Phys. Lett. **97**, 241902 (2010).
7. T. Schröder, F. Gädeke, M. J. Banholzer and O. Benson, New J. Phys. **13**, 055017 (2011).
8. B.D. Gerardot, S. Seidl, P. A. Dalgarno, R. J. Warburton, M. Kroner, K. Karrai, A. Badolato, and P. M. Petroff, Appl. Phys. Lett. **90**, 221106 (2007).
9. A. N. Vamivakas, M. Atatüre, J. Dreiser, S. T. Yilmaz, A. Badolato, A. K. Swan, B. B. Goldberg, A. Imamoğlu, and M. S. Ünlü, Nano Letters **7**, 2892 (2007).
10. G. Wrigge, I. Gerhardt, J. Hwang, G. Zumofen and V. Sandoghdar, Nature Physics **4**, 60 (2008).
11. Q. Wu, G. D. Feke, R. D. Grober, and L. P. Ghislain, Appl. Phys. Lett. **75**, 4064 (1999).
12. H. Benisty, H. De Neve, and C. Weisbuch, IEEE J. Q. E. **34**, 1612 (1998).
13. A. J. Bennett, D. C. Unitt, P. See, A. J. Shields, P. Atkinson, K. Cooper and D. A. Ritchie, Appl. Phys. Lett. **86**, 181102 (2005).

14. G. Ramon, U. Mizrahi, N. Akopian, S. Braitbart, D. Gershoni, T. L. Reinecke, B. D. Gerardot, and P. M. Petroff, Phys. Rev. B **73**, 205330 (2006).
15. Y. Ma, P.E. Kremer, and B. D. Gerardot, J. Appl. Phys. **115**, 023106 (2014).
16. K. J. Vahala, Nature **424**, 839 (2003).
17. L. Sapienza, M. Davanco, A. Badolato, and K. Srinivasan, arXiv, 1503.07141 (2015).
18. E. D. Palik, Handbook of optical constants of solids, academic press (1991).
19. Y. Zhang, Opt. Comm. **266**, 94 (2006).
20. G. V. Trentini, IRE Trans. Antennas Propag. **4**, 666 (1956).
21. Principles of optics: electromagnetic theory of propagation, interference and diffraction of light, Cambridge University Press (1999).
22. D. T. F. Marple, J. Appl. Phys. 35, 1241 (1964).
23. B. Möller, U. Woggon, M. V. Artemyev, and R. Wannemacher, Appl. Phys. Lett. **83**, 2686 (2003).
24. H. Benisty, R. Stanley, and M. Mayer, JOSA A **15**, 1192 (1998).
25. K. S. Chang, S. Y. Min, Y. T. Lee, IEEE Phot. Tech. Lett. **18**, 121(2006).


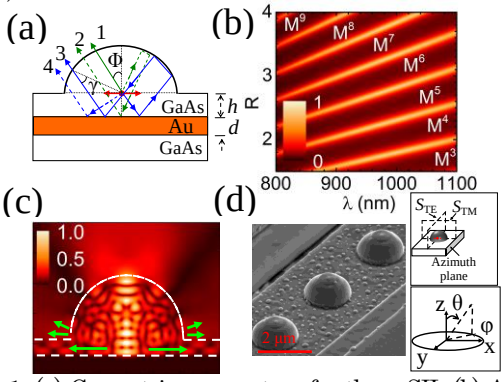


Figure 1: (a) Geometric parameters for the μ-SIL (b) Analytical results for the normalized power sum $E_{rad}$ as function of $R$ and $\lambda$. (c) Cross-section of the electric field inside the micro-SIL for the resonance mode $M_2^7$ ($R$ = 3.8) simulated with 3D-FDTD. Green arrows indicate the leaky modes. (d) Scanning electron micrograph of GaAs μ-SILs fabricated using water-assisted FIB. The insets show the two 2D-FDTD simulation planes ($S_{TE}$ and $S_{TM}$) and the spherical coordinates for the far-field profile.

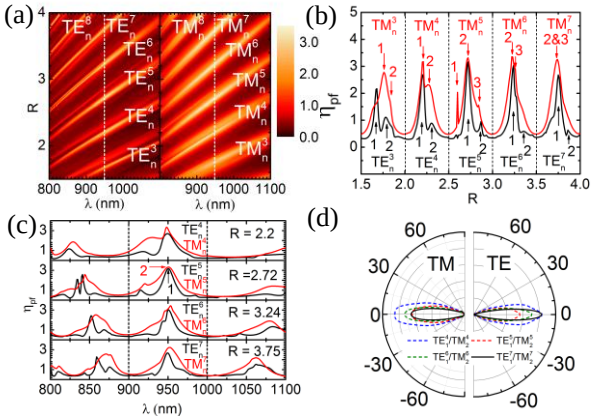


Figure 2: 2D-FDTD simulations of (a) $\eta_{pf}$ as a function of $R$ and $\lambda$ for the *TE* mode (in the $S_{TE}$ plane) and *TM* mode (in the $S_{TM}$ plane); (b) $\eta_{pf}$ as a function of $R$ for $\lambda$ = 950 nm; (c) $\eta_{pf}$ as a function of $\lambda$ for several values of $R$; (d) the far-field distribution for several resonance modes at $\lambda$ = 950 nm.

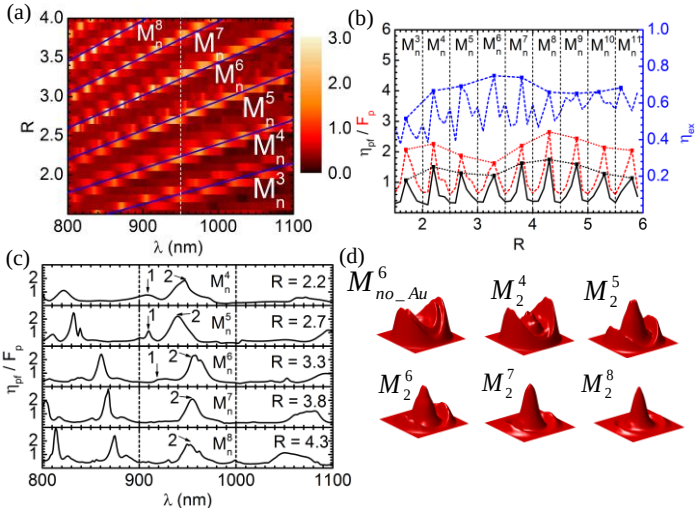


Figure 3: 3D-FDTD simulations of (a) $\eta_{pf}$ as a function of $R$ and $\lambda$; (b) $\eta_{pf}$ (black solid line), $F_p$ (red dashed line) and $\eta_{ex}$ (blue dashed line) as a function of $R$ for $\lambda$ = 950 nm; (c) $\eta_{pf}$ as a function of $\lambda$ for several values of $R$; (d) the far-field distribution for several resonance modes at $\lambda$ = 950 nm. Also shown is the far-field of a mode, $M^6_{no\_Au}$, for a μ-SIL on a bulk sample without back-reflector.

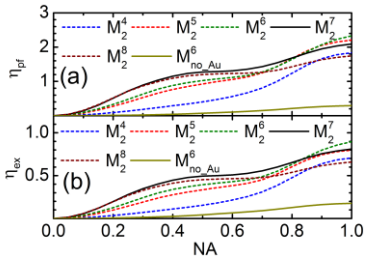


Figure 4: (a) $\eta_{pf}$ and (b) $\eta_{ex}$ as a function of NA for various resonance modes.

| Mode | R | λ (nm) | Δλ (nm) | Q | $F_p$ | $\eta_{pf}$ NA 0.5 | $\eta_{pf}$ NA 0.7 | $\eta_{pf}$ NA 1.0 | $\eta_{ex}$ NA 0.5 | $\eta_{ex}$ NA 0.7 | $\eta_{ex}$ NA 1.0 |
|---|---|---|---|---|---|---|---|---|---|---|---|
| $M_2^4$ | 2.20 | 947 | 22.0 | 41.3 | 2.6 | 0.40 | 0.81 | 1.84 | 0.16 | 0.31 | 0.71 |
| $M_2^5$ | 2.70 | 940 | 19.2 | 48.9 | 2.76 | 0.93 | 1.25 | 2.20 | 0.33 | 0.45 | 0.80 |
| $M_2^6$ | 3.30 | 958 | 18.4 | 52.2 | 2.59 | 1.02 | 1.27 | 2.33 | 0.39 | 0.49 | 0.90 |
| $M_2^7$ | 3.80 | 955 | 16.1 | 59.2 | 2.59 | 1.27 | 1.43 | 2.09 | 0.49 | 0.55 | 0.81 |
| $M_2^8$ | 4.30 | 950 | 19.4 | 48.3 | 2.62 | 1.20 | 1.27 | 1.75 | 0.45 | 0.48 | 0.67 |
| $M^6_{no\_Au}$ | 3.30 | 950 | 60 | 21.4 | 1.62 | 0.04 | 0.15 | 0.29 | 0.04 | 0.09 | 0.18 |

Table 1: Figures of merit for several μ-SIL cavity modes calculated by 3D-FDTD simulations.